Faraday Discussions

Transformations in crystals of DNA-functionalized nanoparticles by electrolytes

Journal:	*Faraday Discussions*
Manuscript ID	FD-ART-05-2023-000109.R1
Article Type:	Paper
Date Submitted by the Author:	15-Jun-2023
Complete List of Authors:	Reinertsen, Roger ; Northwestern University, Materials Science and Engineering Jimenez-Angeles, Felipe; Northwestern University, Materials Science Kewalramani, Sumit; Northwestern University, Materials Science and Engineering Bedzyk, Michael; Northwestern University, Materials Science and Engineering Olvera de la Cruz, Monica; Northwestern University, Materials Science and Engineering

ARTICLE

Transformations in crystals of DNA-functionalized nanoparticles by electrolytes

Received 00th January 20xx,
Accepted 00th January 20xx

DOI: 10.1039/x0xx00000x

Roger John-Erik Reinertsen[a,*], Felipe Jiménez-Ángeles[a,*], Sumit Kewalramani[a], Michael Bedzyk[a], Monica Olvera de la Cruz[a,b,c]

Colloidal crystals have applications in water treatments, including water purification and desalination technologies. It is, therefore important to understand the interactions between colloids as a function of electrolyte concentration. We study the assembly of DNA-grafted gold nanoparticles immersed in concentrated electrolyte solutions. Increasing the concentration of divalent Ca^{2+} ions leads to the condensation of nanoparticles into face-centered-cubic (FCC) crystals at low electrolyte concentrations. As the electrolyte concentration increases, the system undergoes a phase change to body-centered-cubic (BCC) crystals. This phase change occurs as the interparticle distance decreases. Molecular dynamics analysis suggests that the interparticle interactions change from strongly repulsive to short-range attractive, as the divalent electrolyte concentration increases. A thermodynamic analysis suggests that increasing the salt concentration leads to significant dehydration of the nanoparticle environment. We conjecture that the intercolloid attractive interactions and dehydrated states favour the BCC structure. Our results gain insight into salting out of colloids such as proteins as the concentration of salt increases in the solution.

Introduction

Colloidal dispersions of like-charged particles in deionized water are stable due to the particles' mutual electrostatic repulsion; however, the mobile ions in the medium screen the electrostatic interactions, resulting in a decrease in the strength and range of these interactions with increasing salt concentration[1]. The screened Coulombic interactions can be considered using the potential derived in the Derjaguin-Landau-Verwey-Overbeek (DLVO) theory [2-3], which depends on a screening length $\lambda = \kappa^{-1}$. The screening length can be adjusted by changing different parameters in the system. In particular, the inverse of the screening length κ increases by increasing the ions' concentration and valence and decreases by increasing the temperature and the medium dielectric constant. In certain solution ionic conditions, charged particles form highly ordered arrays of particles known as colloidal crystals[4-6].

Like-charged, spherical colloidal particles interacting via repulsive screened Coulombic interactions assemble into different lattice types depending on screening length; typically, larger screening lengths, allowing for "softer", longer-ranged repulsions, favour the body-centered cubic (BCC) structure, while smaller screening lengths, leading to "harder", shorter-ranged interactions, favour the face-centered cubic (FCC) structure [7-9]. Here, we show that nanoparticles functionalized with highly charged flexible ligands, assemble into FCC crystals at low salt concentrations, and BCC crystals at high salt concentrations. This is quite unexpected, as in charged systems, FCC structures do not transition to BCC, including when co-assembled with highly size-asymmetric oppositely charged nanoparticles [10-11]; exceptions typically require specific interactions or the presence of an external field.[4] Our analysis of the present system suggests that water-mediated interactions between the ions and the charges in the nanoparticles are responsible of transforming FCC to BCC as the salt concentration increases.

Some insights into the relative stability of FCC and BCC structures in ligand-coated nanoparticles may be gleaned from experimental observations and phenomenology in systems of particles consisting of hard cores and *neutral* polymer brush shells (grafted particles or diblock copolymer micelles). In these systems, the stability of FCC and BCC structures varies depending on the particle properties. A small ratio of the brush length-to-core radius favours FCC structures, while a large ratio favours BCC micelles [12]. Low surface densities of grafted polymer chains favour BCC structures [13]. The role of the effective softness has been quantified [14-15]. Soft brushes (long and sparse) stabilize second-nearest neighbour interactions in BCC structures. High chain flexibility and large brush-to-core ratios favouring BCC structures also apply to nanoparticle superlattices assembled via DNA-bases pairing [16]. Small nanocrystals grafted with

[a] Department of Materials Science and Engineering, Northwestern University, Evanston, Illinois 60208, USA
[b] Department of Physics, Northwestern University, Evanston, Illinois 60208, USA
[c] Department of Chemistry, Northwestern University, Evanston, Illinois 60208, USA
† e-mail: m-olvera@northwestern.edu
*R. J.-E. R. and F. J.-A. contributed equally, and both are equal first authors to this work.

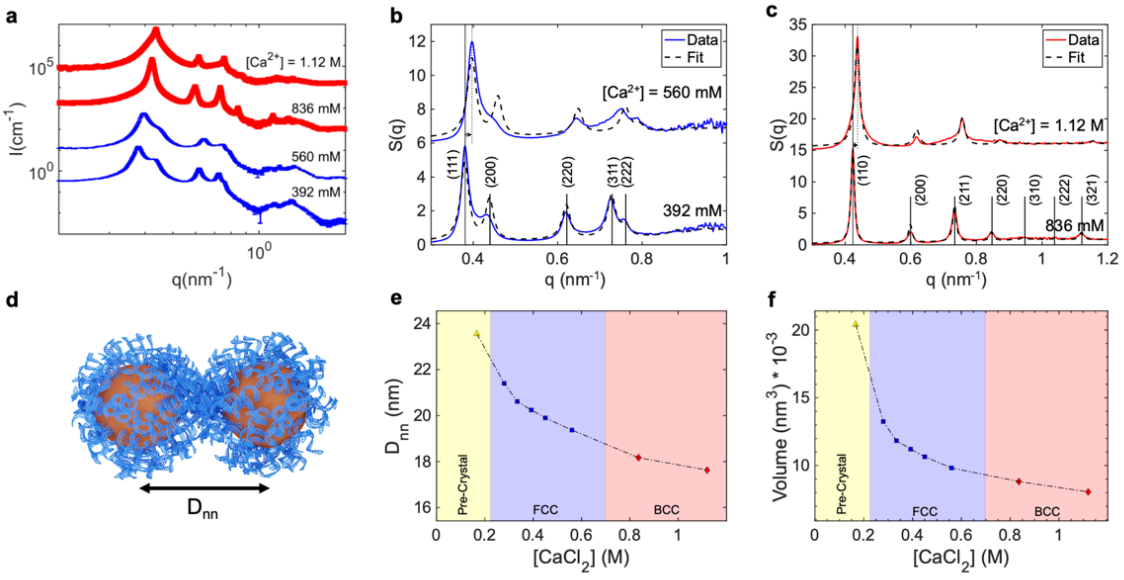

Figure 1 (a) Background-subtracted Small-angle X-ray Scattering data for the DNA-grafted nanoparticles assembled at various $CaCl_2$ concentrations (b, c) Extracted structure factors for the nanoparticle aggregates, compared to model fits for FCC (b) and BCC (c) crystals. (d) A schematic defining the nearest-neighbour interparticle separation, D_{NN}, which the nanoparticles assume in the colloidal crystals (e) A plot of phase and nearest neighbour separation (D_{NN}) as a function of $CaCl_2$ concentration. "Pre-crystal" refers to nanoparticle suspensions with no visible sedimentation, and very weak scattering peaks. (f) A plot of volume per nanoparticle in the structures, as calculated by the lattice parameters and packing efficiencies; the volume per particle does not increase across the FCC-BCC transition.

alkyl ligands favour BCC structures when the ligands are longer [17]. These results are explained in a model by assuming that the "packing frustration" of the ligands decreases in BCC structures. Consequently, a smaller number of chains needs to be compressed or extended to accommodate packing constraints than in the FCC structure [18].

FCC to BCC transitions have been observed in some systems such as diblock copolymer micelles in water upon increasing temperature due to a decrease in the aggregation number of the micelles, thus making the brush sparser (and "softer) [19]. Alkyl-grafted nanocrystals assembled via slow solvent removal [20] [21] transition from FCC to BCC structures as they dry. Lattices of oleic-acid functionalized nanocrystals transition from FCC to BCC structures as a non-solvent (such as ethanol) is added, which should pull solvent away from the ligands, destabilizing the particles[22]. Related studies show that swelling of a nanocrystal lattice with solvent vapor drives a transition from BCC to FCC.[23]

In ligand-coated systems, FCC structure appear to be favourable over BCC structures in the presence of solvents favourable to the ligands. One hypothesis is that the swelling of the alkyl ligands by a solvent makes the particles behave as hard sphere, so the ligands do not deform (or interdigitate) favouring FCC structures [24]. Similar reasoning appears in a molecular dynamics study of nanocrystals suspended in toluene and hexane [25]. Missoni and Tagliazucchi use a molecular theory to show that the presence of solvents in nanoparticle superlattices favours FCC over BCC structures[26]. Extending these considerations to a charged, ion-containing aqueous system would be an exciting step forward.

Here we analyse assembly as a function of the salt concentration in a system consisting of gold nanoparticles (R ~ 4.5 nm) that are densely functionalized by single-stranded (ss-DNA) (~ 65 DNA per Au nanoparticle). The DNA strands were comprised of 35 Thymine bases (T_{35}), which prohibited assembly through base-pairing interactions. We note that the condensation into crystalline lattices and crystal phase transitions in this system are due to electrolyte-mediated effects. We consider monovalent and divalent cations, using NaCl and $CaCl_2$ electrolytes. In solutions containing only NaCl, we do not observe nanoparticle aggregation, in agreement with expectation from the interaction potential obtained from Inverse Lattice Boltzmann simulations of double-stranded (ds)-DNA functionalized nanoparticles in NaCl electrolytes.[27] In contrast, ssDNA-coated nanoparticles were previously found to assemble into FCC lattices above a threshold concentration of divalent ions [28]. In that study, our molecular dynamics (MD) simulations on ds-DNA capped nanoparticles in divalent ions, without explicit water revealed that FCC crystals at low divalent ion concentration arise due to interparticle attractions of longer range than expected by ion bridging. Here, we find that contrary to other systems of like-charged colloids, the FCC phase that appears at a low salt concentration of divalent ions transforms to the BCC phase as the ions' concentration increases. Based on all-atom MD simulations, we hypothesize that dehydration on nanoparticles at high electrolyte concentration leads to the phase transformation from FCC to BCC.

The paper is organized as follows: First, we present the results from our experimental measurements and our analysis using molecular dynamics simulations. We investigate the interface of the nanoparticle and DNA with the electrolyte. A brief description of the

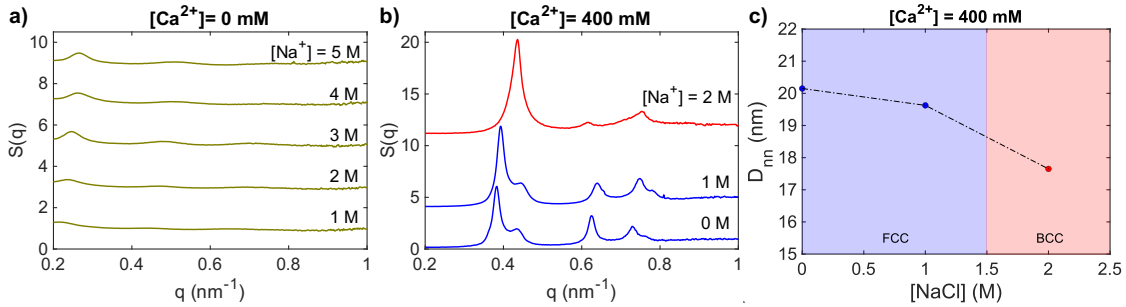

Figure 2 (a,b) Extracted structure factors for the DNA-grafted nanoparticles at various NaCl concentrations, with the solution also containing (a) 0 mM $CaCl_2$ and (b) 400 mM $CaCl_2$ (c) A plot of phase and nearest neighbour separation (D_{NN}) as a function of $CaCl_2$ concentration.

experimental and simulation techniques is included in the results' discussion as well as the relation of our work to the structure of the water and ions around DNA. Further details are supplied in the Methods section. Some conclusions and perspectives are included at the end of the manuscript.

Results

Experimental Results

Single-stranded (ss)-DNA-functionalized gold nanoparticle conjugates (DNA-NP) have a high net negative charge, which results in repulsive electrostatic interactions between particles. These repulsions prevent the nanoparticles' precipitation even in concentrated NaCl solutions. By contrast, in the presence of sufficient concentrations of Ca^{2+} ions (as provided by the addition of $CaCl_2$), attractive forces drive the precipitation of the conjugates within minutes. In-situ small-angle X-ray scattering (SAXS) measurements reveal that the conjugates pack into FCC lattice just above a threshold $CaCl_2$ concentration of ~ 280 mM (Fig. 1a-b). SAXS also shows that increasing the $CaCl_2$ concentration drives the compression of the lattices (Fig. 1b, e). Above 700 mM $CaCl_2$, the aggregates transition into BCC crystals, with the interparticle separation continuing to decrease with added salt (Fig. 1c, e). While the BCC phase features a lower packing efficiency than the FCC phase, we calculate that the volume per particle within the lattices continues to decrease across the transition (Fig. 1f). We note here that our previous study on non-base pairing, ssDNA-grafted nanoparticles assembled via Ca^{2+} cations instead displayed a transition from FCC to an amorphous, glassy state at higher $CaCl_2$ concentration.[28] We attribute this difference to more homogenous DNA coverages in the present study, as well as greater intervals between sample preparation and measurement enabling additional growth of colloidal crystals.

The monovalent salt, NaCl, is unable to induce the precipitation of the DNA-NP at any accessible concentration in water (Fig. 2a), with SAXS patterns only displaying very weak scattering peaks. However, nanoparticle superlattices formed at 400 mM $CaCl_2$ contract upon increasing the NaCl concentration of the system up to 1 M. Additionally, increasing [NaCl] to 2 M induces the same FCC-to-BCC transition observed upon sufficient increase in [$CaCl_2$] (Fig. 2b-c). These observations suggest that while divalent ions are essential for inducing DNA-NP crystallization, lattice compression and structural phase transitions are determined by the overall solution salt content. Based upon these observations, we hypothesize that increasing the solution ionic strength modifies the interactions between the grafted DNA and the Ca^{2+} cations. The addition of salt strengthens the attractive interactions between Ca^{2+} and the DNA-phosphate groups and the nanoparticles, and weakens the electrostatic repulsion between the anionic phosphates. Both these effects lead to denser nanoparticle assemblies. An effect may be that the salt dehydrates the DNA and favours denser packing of nanoparticles via a mechanism analogous to the salting out of proteins [29]. In the next section, we employ molecular dynamics simulations to analyse these hypotheses.

Molecular Simulation Results

We performed all-atom explicit solvent molecular dynamics (MD) simulations using the setup shown in Figure 3. The system consists of a DNA-grafted gold nanoparticle immersed in an electrolyte solution made of Ca^{2+} and Cl^- ions. The simulation box is replicated multiple times by applying periodic boundary conditions in the *x*-, *y*-, and *z*-directions. The box sizes considered in our study allow the interaction between the nanoparticles in the neighbouring image boxes. Therefore, the simulation box is considered a unit in a three-dimensional crystalline system. We explored different ion concentrations. The system details are provided in the Methods section.

The DNA molecules are grafted to the nanoparticle's surface; however, they adopt different configurations around the nanoparticle as a function of the electrolyte concentration. Fig. 4a shows the density profiles of the DNA molecules as a function of the distance to the nanoparticles' centre. All the DNA profiles have a common peak at $r \approx 2.7$ nm due the grafting on the nanoparticle's surface, and a second peak at $r \approx 3.3$ nm. At $r \gtrsim 3.3$ nm, we see significantly different behaviours of the grafted DNA molecules at different electrolyte concentrations. At the two highest electrolyte concentrations a third peak appears at about $r \approx 3.8$ nm; the higher the electrolyte concentration, the sharper the third peak becomes. Interestingly, at lower electrolyte concentrations ([$CaCl_2$] ≤ 1.2 M), the DNA extends beyond $r \gtrsim 3.8$ nm, decaying monotonically, whereas at the higher electrolyte concentrations the profiles do not extend past this value. This behaviour indicates that the electrolyte

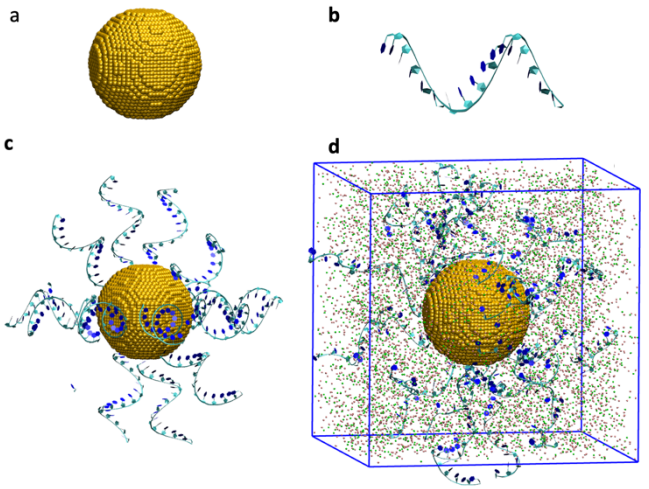

Figure 3 Simulation setup employed to analyse the chemical equilibrium of a dense phase made of DNA-grafted gold nanoparticles and $CaCl_2$ ions reservoir. (a) Nanoparticle of 4.5 nm of diameter, (b) all-atom model of a single-stranded DNA molecule made of 17 T-bases, (c) composite system consisting of 18 single-stranded DNA molecules grafted on the surface of the nanoparticle, and (d) simulation box containing a grafted DNA nanoparticle immersed in an electrolyte solution made of Ca^{2+} and Cl^- ions. Water is including explicitly in the system (not shown). Note that due to computational constraints, the DNA-NP in simulations have been scaled down by a factor of ~2. The number of DNA per Au nanoparticle is correspondingly reduced to roughly match the DNA grafting density in experiments.

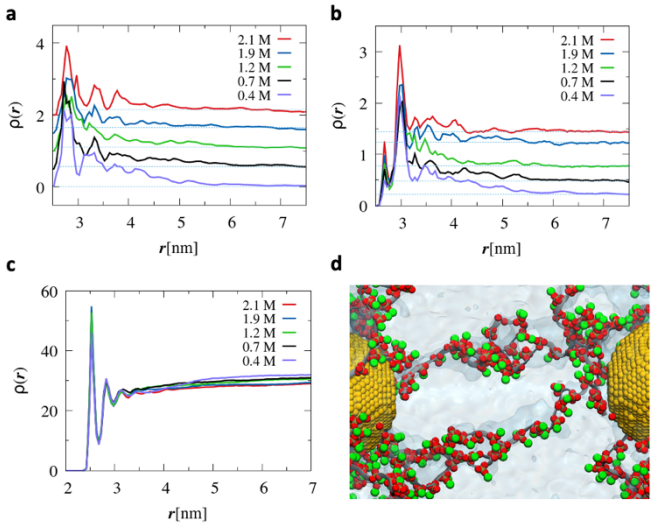

Figure 4 Structure of DNA, ions, and water around the nanoparticle. Density profile of (a) the DNA molecules, (b) Ca^{2+} ions, and (c) water as a function of the distance to the nanoparticle's centre. The DNA density profiles are calculated using the P atom of the PO_4 group of the DNA molecules (see Figure 3b). To aid visualization, the DNA density profiles are shifted upwards by 0.5 with respect to the contiguous profile; the DNA density profile at 0.4 M is not shifted. In the Ca^{2+} profiles, the shifts result naturally from the different concentrations. The line colours represent different $CaCl_2$ molar concentrations. The density units are number of particles/nm^3. The light-blue line is included to show when the profiles reach a uniform value. (d) Instantaneous snapshot of the simulation box showing the aqueous environment around the DNA-grafted nanoparticle. The nanoparticle is shown in yellow, Ca^{2+} ions within 0.5 nm from the P atom are in green, and the DNA backbone is shown as a grey ribbon. The PO_4 groups from DNA are displayed as spheres; P: ochre, and O: red. The image is produced using two contiguous image boxes that self-interact through the DNA strands.

concentration modifies the correlation of the DNA molecules with the nanoparticle's surface. At low electrolyte concentrations the DNA molecules are correlated at longer distances whereas at high concentrations the DNA molecules are more structured near the nanoparticles surface.

By analysing the Ca^{2+} distribution around the nanoparticle, we notice interesting changes as a function of the electrolyte concentration. The density profiles in Figure 4b show a peak at around $r \approx 2.5$ nm which implies the adsorption of Ca^{2+} ions on the nanoparticle's surface. This peak is due to the electrostatic attraction of the grafted Ca^{2+} cations by the DNA on the surface. The ionic correlations enhance the Ca^{2+} adsorption on the nanoparticle's surface, therefore, the adsorption is small at the lowest concentration and increases as the ionic concentration increases. A secondary peak is at $r \approx 3$ nm and some ionic structure between $3\,\text{nm} \lesssim r \lesssim 4\,\text{nm}$ because of the interaction between the Ca^{2+} and the DNA molecules. The density profiles show that the correlation length decreases as the electrolyte concentration increases. For example, at 0.2 M the ionic density profile decay monotonically from $r \approx 4$ nm and becomes uniform at about $r \approx 6$ nm, whereas at 2.1 M the profile is uniform from $r \approx 4.5$ nm. These changes in the correlation length and ionic structure around the nanoparticle impact the overall interaction between the nanoparticles.[27, 30]

Water mediates the interactions of biomolecules with ions and other molecules.[31] In Figure 4c, we analyse the aqueous environment using the water density profile. The water density profiles show a main peak at $r \approx 2.5$ nm that increases as the $CaCl_2$ concentration increases, and three more peaks of decreasing height as the distance to the nanoparticle's surface increases. Then, the density profiles tend to a constant value that is reached at a closer distance from the surface as the electrolyte concentration increases. For the highest electrolyte concentration (2.1 M), the water density plateau is reached at $r \approx 4.5$ nm, whereas at the lowest concentration (0.4 M) the plateau is reached at a $r \approx 6.5$ nm. Fig. 4d shows an instantaneous configuration of the DNA strands and the ionic environment that mediates the nanoparticles' interaction in the dense phase.

The correlation between the nanoparticles and the ions occurs primarily via the DNA charged groups. In Fig. 5a we investigate the correlations between the DNA PO_4 groups and the Ca^{2+} ions using the radial distribution functions (RDF) at different electrolyte concentrations. We find that the PO_4 groups strongly adsorb the Ca^{2+} ions, which is seen as a peak in the RDF profiles at about $r \approx 0.3$ nm.

Furthermore, we observe other peaks at $r \approx 0.6$, 0.8, and 1.25 nm caused by the crossed correlation via neighbouring PO_4 groups in the DNA molecule. By increasing the electrolyte concentration, the crossed correlations gradually decrease. Consequently, at 2.1 M the third peak at $r \approx 1.25$ nm, almost disappears, and the profile is uniform at long distances. At the lowest concentration (0.4 M) the correlations between the PO_4 groups and the Ca^{2+} ions are of a much longer range than 2 nm.

It is worth noticing that the grafted DNA nanoparticle enhance the correlations between the ions. In Fig. 5b, the RDF profiles between Ca^{2+} ions peak at about $r \approx 0.47$ nm, also observed in the bulk solution. At the lowest electrolyte concentration, the secondary peak

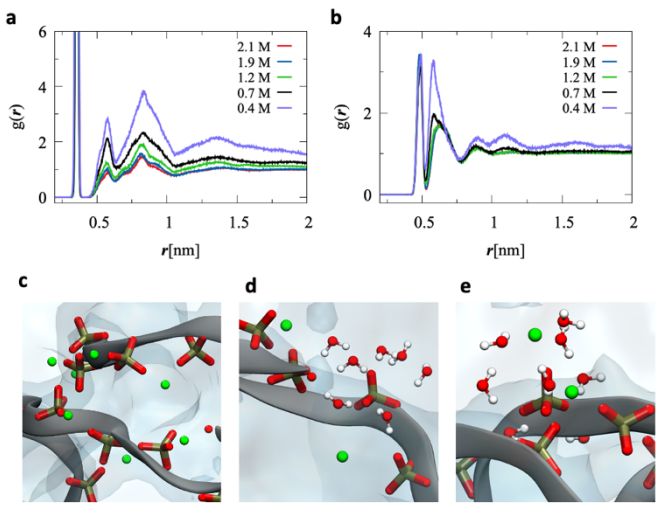

Figure 5 Radial distribution functions (a) PO^{-}_{4} - Ca^{2+} and (b) Ca^{2+} - Ca^{2+} at different $CaCl_2$ concentrations. Snapshots of the environment around the PO_4 groups of DNA (c) Ca^{2+} ions in the system at 2.1 M, and water molecules and Ca^{2+} ions near a PO_4 group in a system at (b) 0.4 M and (e) 2.1M.

at $r \approx 0.6$ nm is much more pronounced in the presence of the DNA molecules than in bulk. In addition, the ion-ion correlations are of longer range at the lowest concentration than at the higher ones. Fig. 5c-e show snapshots of the ions and water around the PO_4 DNA groups. We can see that the Ca^{2+} ions coordinate with multiple PO_4 groups and induce the bridging between them. Fig. 5d-e shows that the PO_4 groups are better hydrated at low than at high electrolyte concentrations because the Ca^{2+} remove water from the PO_4 groups.[32]

In summary, the DNA molecules adopt extended configurations at low electrolyte concentrations, and they become more compact and layered near the nanoparticle's surface at high concentrations. Similarly, the range or spatial extension of ionic correlations reduces with increasing electrolyte concentration. Furthermore, by increasing the salt concentration in the system, the Ca^{2+} ions replace the hydration water around the DNA chains. These dehydrated (or less-hydrated) ligands lead to changes in the effective nanoparticles' interaction favour configurations that better accommodate the BCC structure. In other words, a low electrolyte concentration favours the FCC phase, whereas the BCC is more favourable at high electrolyte concentrations.

A change in the separation distance D_{nn} implies a change in the number of water molecules per unit cell. Therefore, the equilibrium separation distance D_{nn} between the nanoparticles results from a balance in the interaction forces and the chemical equilibrium between the crystal and the surrounding ions reservoir. *Hence, we analyze the stable hydration scenarios of the nanoparticles as a function of the $CaCl_2$ concentration.* We consider the system outlined in Fig. 3, and three hydration states represented by the number of water molecules in the box, N_w = 45000, 55000, and 70000. The corresponding box size varies from L =11.5 nm to L =13.5 at the lowest and highest hydration, respectively.

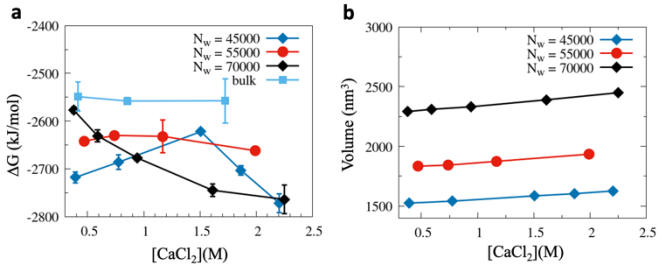

Figure 6 (a) Gibbs free change due to inserting a triplet consisting of one Ca^{2+} ion and two Cl^{-} ions into the simulation box containing one DNA grafted nanoparticle, and (b) equilibrium simulation box Volume. The calculations are performed as a function of the $CaCl_2$ concentration and at different hydration states defined by the number of water molecules N_w in the simulation box.

The equilibrium ion concentration in the reservoir and the nanoparticle dense phase are determined by the thermodynamic equilibrium conditions, namely, $p^{\alpha} = p^{\beta}$ and $\mu^{\alpha}_{i} = \mu^{\beta}_{i}$ where p and μ_i are, respectively, the pressure and the chemical potential of species i (see Phase Equilibrium sub-section in Methods). The superscripts α and β designate the nanoparticles' dense phase and the aqueous phase (β), respectively. The chemical potential is expressed in terms of the Gibbs free energy as

$$\mu_i = \left(\frac{\partial G}{\partial N_i}\right)_{p,T,N_{j\neq i}} \quad (1)$$

where N_i is the number of particles of species i and n is the number of species in the system. To maintain the system electroneutrality during the free energy calculation, we consider inserting an artificial 'molecule' with no internal bonds formed by one Ca^{2+} ion and two Cl^{-} ions. We refer to this artificial molecule as a *triplet*. We calculate the chemical potential as the change of the Gibbs free energy by introducing the 'molecule' into the system as

$$\mu_i = \left(\frac{\Delta G}{\Delta N_i}\right)_{p,T,N_{j\neq i}} = G(T,p,N_1,\ldots,N_i,\ldots,N_n) - G(T,p,N_1,\ldots,N_i - 1,\ldots,N_n) \quad (2)$$

The change of the free energy is calculated using the slow-growth method in thermodynamic integration[33-34] to transform the system from state A to state B as follows

$$G^B(T,p) - G^A(T,p) = \Delta G = \int_0^1 \left\langle \frac{\partial H}{\partial \lambda} \right\rangle_{\lambda} d\lambda \quad (3)$$

λ is a coupling parameter that varies from 0 to 1 to modulate the interaction between the target molecule and the medium that is gradually turned in the system's Hamiltonian, such that the interaction between the medium and the molecule is switched off at state A (λ=0) and is on in state B (λ=1).

Figure 6a shows the change in the Gibbs free energy by inserting a triplet into the system as a function of the electrolyte concentration

and at three different hydration states, namely, $N_w = 45000$, 55000, and 70000. At the highest hydration state (N_w =70000), the change in Gibbs free energy decreases by increasing the electrolyte concentration, implying that the insertion of a new triplet into the system is favorable at this hydration state. For the two lower hydration states, the change in the Gibbs free energy shows states that are as likely as the states with the highest hydration. Hence, our analysis shows that the dehydrated states are energetically favorable as the electrolyte concentration increases. In Figure 6b, the simulation box volume shows sensitive increments by increasing the $CaCl_2$ concentration. By changing the number of water molecules, the changes in the volume are significantly more pronounced. This simple analysis supports our hypothesis about a significant dehydration by increasing the salt concentration.

We analyzed the changes in the Gibbs free energy in a system consisting of a $CaCl_2$ electrolyte solution. The Gibbs energy changes by inserting a triplet in bulk are higher than in the system containing the grafted DNA nanoparticle. Therefore, our simulation method is limited to determining the equilibrium conditions between the reservoir and the crystalline system. We speculate that this limitation is due to a missing concentration of nanoparticles, free DNA, or other components in the reservoir that are present in the real system.

Conclusions

In summary, we have presented a system in which nanoparticles grafted with highly charged polyelectrolytes form lattices of different symmetries depending on salt content. While divalent cations are necessary to induce the attractive forces that stabilize the condensed states, increasing the salinity of the solution with divalent or monovalent salts drives contraction of the aggregates, as well as FCC to BCC phase transitions. We hypothesize that the additional salt dehydrates the grafted DNA, strengthening phosphate-cation interactions, as well as more compact, structured DNA conformations amenable to the BCC structures, as evidenced by our molecular dynamics studies. Taken together, these results provide insight on how electrolytes influence charged biomolecule hydration, and demonstrate how these factors can be utilized to produce systems which actuate in response to varied ionic conditions. Our results also demonstrate the importance of surface-electrolyte interactions in concentrated electrolytes.

Methods

DNA Synthesis

We select the sequence 5'-T_{35}-C_3SH- 3' to prepare grafted DNA with a minimal propensity for base-pairing and forming secondary structure. The 3' propyl-thiol terminated oligonucleotides are synthesized using a MerMade solid-state controlled pore glass (CPG) DNA synthesizer (BioAutomation) via phosphoramidite chemistry. Following the synthesis, the DNA is released from the CPG beads using a mixture of methylamine and NH_4OH (1:1 volume ratio) at 55°C for 30 minutes. The DNA is then transferred to DI water and purified via reverse-phase high-performance liquid chromatography (RP-HPLC). The 5'-DMT group, which enables separation via HPLC, is then removed via a reaction with 20% acetic acid and subsequent extraction with ethyl acetate. The purity and molecular weight of the synthesized sequences are verified with matrix-assisted laser desorption/ionization time-of-flight spectroscopy (MALDI-TOF, from Bruker). The concentration of the DNA solutions is determined via UV-Vis spectroscopy at 260 nm.

Gold nanoparticle functionalization

The thiol-terminated oligonucleotides are grafted to the surfaces of the colloidal gold nanoparticles following established methods[35] . Briefly, the thiolated DNA molecules are reduced in 100 mM dithiothreitol (DTT) maintained at an approximate pH of 8 via phosphate buffer. Following the reaction for 30-60 minutes, the DNA is transferred to the water via purification through size-exclusion NAP5 columns. The reduced DNA is added to colloidal AuNP solutions of about 10 nM at an approximate ratio of 372 DNA/AuNP. The solutions are incubated overnight. Sodium chloride (NaCl) and small quantities of 0.1% Sodium Dodecyl Sulfate (SDS) are then slowly added to the solution for 8 hours until a final concentration of 1 M NaCl is achieved. This process enables high grafting density on the nanoparticles. Unbound DNA is removed via centrifugation using 50 kDa spin filters. To minimize the presence of NaCl, unbound DNA, and SDS in the final nanoparticle stocks, we transfer the DNA-AuNPs to DI water and purify them through three centrifugation rounds. Final DNA-AuNP concentrations are determined by applying Beer's Law to the UV-Vis-measured absorbance of the AuNP at 520 nm.

Oligreen Assay

The number of DNA strands per particle is measured using[36] a Quant-iT Oligreen Assay from Invitrogen. To dissolve the gold cores and release the DNA into the solution, suspensions of known DNA-AuNP are briefly reacted in 20 mM KCN solution at 50°C. The liberated DNA is then stained with the Oligreen fluorescent dye (diluted in TE buffer as per manufacturer instructions). The fluorescence of these solutions at 480 nm is measured using a Biotek Cytation 5 imaging reader. These values are compared to those measured for Oligreen-stained 5'-T_{35}-C_3SH- 3' solutions of various known concentrations. Comparison to the calibration curve's fluorescence allows for quantifying the amount of DNA associated with a known quantity of DNA-AuNPs, thus determining average loading.

Sample Preparation

To prepare samples with high salt concentrations, saturated solutions of $CaCl_2$ and NaCl in water were prepared at ~22°C and allowed to equilibrate with precipitated hydrate phase at least 12 hours before use. Solutions were prepared using Calcium Chloride Dihydrate (99.5% purity, Sigma-Aldrich) and Sodium Chloride (99.99% purity Suprapur®, Millipore-Sigma). Samples for SAXS analysis were prepared in total volumes of 30-50 µL, with final DNA-

AuNP concentrations of 50 nM, and the $CaCl_2$ solution being the final component added to the mixture. Following the addition of the salt, the solution was promptly (within 60 seconds) homogenized via pipette and transferred to 1.0 mm or 1.5 mm quartz glass capillaries (Charles Supper). The capillaries were then sealed with epoxy, and 24-36 hours were allowed to elapse prior to measurement.

X-ray measurements

SAXS measurements on nanoparticle suspensions were conducted at beamline 5ID-D of the Advanced Photon Source. To compensate for the X-ray attenuation of the concentrated salt solutions, the X-ray energy was tuned to 17 keV (0.7293 Å wavelength). The scattered intensities were measured simultaneously using three Rayonix CCD detectors positioned ~0.2m, ~1.0m, and ~7.5m from the sample, allowing for data collection over the range 0.02 $nm^{-1} < q < 30\ nm^{-1}$. The X-ray spot size on the sample position was 0.25 mm x 0.25 mm, and the incident flux was ~ 3×10^{11} photons/s. Capillary samples were mounted horizontally on a translating capillary stage. Samples were scanned for sets of three 5-second exposures, with the capillaries being translated continuously at 0.508 mm/s during measurement to minimize radiation damage. The 2D data was reduced to 1D intensity profiles via azimuthal integration (using GSAS-II), following corrections for polarization, detector solid angle, and transmission.

Phase Equilibrium

The thermodynamic equilibrium of the system is governed by the exchange of water and ions between the nanoparticles' dense phase and the surrounding reservoir. Hence, here we revise the thermodynamics of phase equilibrium in multicomponent systems. We will employ this formulation to develop a method to investigate the system formed by the DNA-grafted gold nanoparticles immersed in a multivalent ions solution. Let us consider a system formed by K different species (which maybe atoms, ions, and molecules), of number density $\rho_i = \frac{N_i}{V}$ and chemical potential μ_i; being N_i the number of particles of species *i*, *V* the total volume, and $i = 1, \dots, K$. In the phase equilibrium, the components are divided into *J* regions (phases) with corresponding number densities $\rho_i^{\alpha_1}$, $\rho_i^{\alpha_2}, \dots, \rho_i^{\alpha_J}$, where the subscript and superscript designate the species and the phase, respectively. In general, $\rho_i^{\alpha_1} \neq \rho_i^{\alpha_2} \neq \cdots \rho_i^{\alpha_J}$. The phase equilibrium is determined by the thermal equilibrium,

$$T \equiv T^{\alpha_1} = T^{\alpha_2} = \cdots = T^{\alpha_J}, \quad (4)$$

the mechanical equilibrium,

$$p \equiv p^{\alpha_1} = p^{\alpha_2} = \cdots = p^{\alpha_J}, \quad (5)$$

and the chemical equilibrium

$$\mu_i \equiv \mu_i^{\alpha_1} = \mu_i^{\alpha_2} = \cdots = \mu_i^{\alpha_J} \quad (6)$$

T, p, and μ_i represent the temperature, the pressure, and the chemical potential of *i*-th species, respectively; the superscript designates the phase. In processes at constant *p* and *T*, the Gibbs free energy is the thermodynamic potential that is minimized in equilibrium,

$$dG = -SdT + Vdp + \sum_{i=1}^{J} \mu_i \mathrm{d}N_i \quad (7)$$

At constant *V* and *T*, the corresponding thermodynamic potential is the Helmholtz free energy, given by

$$dF = -SdT - pdV + \sum_{i=1}^{J} \mu_i \mathrm{d}N_i \quad (8)$$

The chemical potential in terms of the Gibbs free energy is given as

$$\mu_i = \left(\frac{\partial G}{\partial N_i}\right)_{T,P,N_{j\neq i}} \quad (9)$$

In terms of the Helmholtz free energy, the chemical potential is given as

$$\mu_i = \left(\frac{\partial F}{\partial N_i}\right)_{T,V,N_{j\neq i}} \quad (10)$$

In our study, we will deal with small changes due to the insertion/deletion of one ionic triplet in an aqueous phase. Therefore, $pdV \approx Vdp \approx 0$, and $\Delta F \approx \Delta G$.

Molecular Dynamics Simulations

Classical all-atom explicit solvent MD simulations are conducted using the CHARM force field parameters[37-38] to model the system's interactions. The dense phase is represented by a unit cell that contains a single DNA-grafted spherical nanoparticle replicated in x, y, and z directions using periodic boundary conditions. The spherical nanoparticle is 4.5 nm of diameter, approximately, and is made of uncharged non-polarizable atoms. The spherical nanoparticle surface is decorated using 18 single-strand DNA chains formed of 17 thymine bases bearing a total charge of -16e distributed along its length; e is the positive elementary charge. The structure of DNA is built using the conformational parameters taken from experimental fiber-diffraction studies[39]. The nanoparticle's shape is maintained using harmonic-potential interactions between neighboring atoms. The DNA chains are attached to the nanoparticle's surface using a harmonic potential between a carbon atom at the end of the DNA strand and an atom at the nanoparticle's surface. The decorated

spherical nanoparticle is placed at the center of a cubic simulation of side L, including (N +144) Ca2+ ions 2N Cl ions, and Nw water molecules; the extra 144 Ca2+ ions are necessary to maintain the system electroneutrality. The simulations are performed using the package GROMACS[40-41]. To model the electrostatic and van-der-Waals interactions in the system, we employ the CHARM force field parameters[37-38] to model the system's interactions. The electrostatic interactions are calculated the PME algorithm. To equilibrate the molecules in bulk and at the interface we performed microsecond MD simulations using a time-step of 2.5 fs at T = 298 K. The temperature is controlled using the Nose-Hoover thermostat, and the pressure is maintained using the Parrinello-Rahman barostat.

Author Contributions

M. O. d. l. C. and M. B. conceived the idea and designed the research. R J.-E. R and S. K. performed the experimental measurements. F. J.-A. performed the simulations. All the authors contributed to the analysis, discussions, and drafting of the manuscript.

Conflicts of interest

There are no conflicts to declare.

Acknowledgements

This work was funded by the Department of Energy (DOE), Office of Basic Energy Sciences under Contract No. DE-FG02-08ER46539. This work made use of the IMSERC MS facility at Northwestern University, which has received support from the Soft and Hybrid Nanotechnology Experimental (SHyNE) Resource (NSF ECCS-2025633), the State of Illinois, and the International Institute for Nanotechnology (IIN). Portions of this work were performed at the DuPont-Northwestern-Dow Collaborative Access Team (DND-CAT) located at Sector 5 of the Advanced Photon Source (APS). DND-CAT is supported by Northwestern University, The Dow Chemical Company, and DuPont de Nemours, Inc. This research used resources of the Advanced Photon Source, a U.S. Department of Energy (DOE) Office of Science User Facility operated for the DOE Office of Science by Argonne National Laboratory under Contract No. DE-AC02-06CH11357. We thank Steven Weigand of DND- CAT for assistance with the SAXS setup and data reduction, as well as the Mirkin Lab of Northwestern University for allowing our use of their facilities, in particular Jennifer Delgado, Kaitlin Landy, and Vinzenz Mayer for assistance with oligonucleotide synthesis and purification.

References

1. Russel, W. B.; Russel, W.; Saville, D. A.; Schowalter, W. R., *Colloidal dispersions*. Cambridge university press: 1991.
2. Verwey, E. J. W., Theory of the Stability of Lyophobic Colloids. *The Journal of Physical and Colloid Chemistry* **1947,** *51* (3), 631-636.
3. Derjaguin, B.; Landau, L., Theory of the stability of strongly charged lyophobic sols and of the adhesion of strongly charged particles in solutions of electrolytes. *Progress in Surface Science* **1993,** *43* (1), 30-59.
4. Yethiraj, A.; van Blaaderen, A., A colloidal model system with an interaction tunable from hard sphere to soft and dipolar. *Nature* **2003,** *421* (6922), 513-517.
5. Gast, A. P.; Russel, W. B., Simple Ordering in Complex Fluids. *Physics Today* **1998,** *51* (12), 24-30.
6. Thomas, P., Crystallization kinetics of repulsive colloidal spheres. *Journal of Physics: Condensed Matter* **1999,** *11* (28), R323.
7. Robbins, M. O.; Kremer, K.; Grest, G. S., Phase-Diagram and Dynamics of Yukawa Systems. *J Chem Phys* **1988,** *88* (5), 3286-3312.
8. Kremer, K.; Robbins, M. O.; Grest, G. S., Phase-Diagram of Yukawa Systems - Model for Charge-Stabilized Colloids. *Phys Rev Lett* **1986,** *57* (21), 2694-2697.
9. Sirota, E. B.; Ouyang, H. D.; Sinha, S. K.; Chaikin, P. M.; Axe, J. D.; Fujii, Y., Complete Phase-Diagram of a Charged Colloidal System - a Synchrotron X-Ray-Scattering Study. *Phys Rev Lett* **1989,** *62* (13), 1524-1527.
10. Bian, T.; Gardin, A.; Gemen, J.; Houben, L.; Perego, C.; Lee, B.; Elad, N.; Chu, Z.; Pavan, G. M.; Klajn, R., Electrostatic co-assembly of nanoparticles with oppositely charged small molecules into static and dynamic superstructures. *Nature Chemistry* **2021,** *13* (10), 940-949.
11. Lin, Y.; Olvera de la Cruz, M., Sublattice melting in binary superionic colloidal crystals. *Physical Review E* **2020,** *101* (3), 032603.
12. Mcconnell, G. A.; Gast, A. P.; Huang, J. S.; Smith, S. D., Disorder-Order Transitions in Soft-Sphere Polymer Micelles. *Phys Rev Lett* **1993,** *71* (13), 2102-2105.
13. Yun, H.; Yu, J. W.; Lee, Y. J.; Kim, J. S.; Park, C. H.; Nam, C.; Han, J.; Heo, T. Y.; Cho, S. H.; Lee, D. C.; Lee, W. B.; Stein, G. E.; Kim, B. J., Symmetry Transitions of Polymer-Grafted Nanoparticles: Grafting Density Effect. *Chem Mater* **2019,** *31* (14), 5264-5273.
14. Yun, H.; Lee, Y. J.; Xu, M.; Lee, D. C.; Stein, G. E.; Kim, B. J., Softness- and Size-Dependent Packing Symmetries of Polymer-Grafted Nanoparticles. *Acs Nano* **2020,** *14* (8), 9644-9651.
15. Boles, M. A.; Talapin, D. V., Many-Body Effects in Nanocrystal Superlattices: Departure from Sphere Packing Explains Stability of Binary Phases. *J Am Chem Soc* **2015,** *137* (13), 4494-4502.
16. Thaner, R. V.; Kim, Y.; Li, T. I. N. G.; Macfarlane, R. J.; Nguyen, S. T.; Olvera de la Cruz, M.; Mirkin, C. A., Entropy-Driven Crystallization Behavior in DNA-Mediated Nanoparticle Assembly. *Nano Letters* **2015,** *15* (8), 5545-5551.
17. Korgel, B. A.; Fitzmaurice, D., Small-angle x-ray-scattering study of silver-nanocrystal disorder-order phase transitions. *Phys Rev B* **1999,** *59* (22), 14191-14201.
18. Goodfellow, B. W.; Yu, Y. X.; Bosoy, C. A.; Smilgies, D. M.; Korgel, B. A., The Role of Ligand Packing Frustration in Body-Centered Cubic (bcc) Superlattices of Colloidal Nanocrystals. *J Phys Chem Lett* **2015,** *6* (13), 2406-2412.
19. Lodge, T. P.; Bang, J.; Park, M. J.; Char, K., Origin of the thermoreversible fcc-bcc transition in block copolymer solutions. *Phys Rev Lett* **2004,** *92* (14).
20. Weidman, M. C.; Smilgies, D. M.; Tisdale, W. A., Kinetics of the self-assembly of nanocrystal superlattices measured by real-time in situ X-ray scattering. *Nat Mater* **2016,** *15* (7), 775-+.
21. Schmitt, J.; Hajiw, S.; Lecchi, A.; Degrouard, J.; Salonen, A.; Imperor-Clerc, M.; Pansu, B., Formation of Superlattices of Gold Nanoparticles Using Ostwald Ripening in Emulsions: Transition from fcc to bcc Structure. *J Phys Chem B* **2016,** *120* (25), 5759-5766.
22. Lee, B.; Littrell, K.; Sha, Y. C.; Shevchenko, E. V., Revealing the Effects of the Non-solvent on the Ligand Shell of Nanoparticles and Their Crystallization. *J Am Chem Soc* **2019,** *141* (42), 16651-16662.

23. Bian, K. F.; Choi, J. J.; Kaushik, A.; Clancy, P.; Smilgies, D. M.; Hanrath, T., Shape-Anisotropy Driven Symmetry Transformations in Nanocrystal Superlattice Polymorphs. *Acs Nano* **2011,** *5* (4), 2815-2823.
24. Goodfellow, B. W.; Korgel, B. A., Reversible Solvent Vapor-Mediated Phase Changes in Nanocrystal Superlattices. *Acs Nano* **2011,** *5* (4), 2419-2424.
25. Kaushik, A. P.; Clancy, P., Solvent-driven symmetry of self-assembled nanocrystal superlatticesA computational study. *J Comput Chem* **2013,** *34* (7), 523-532.
26. Missoni, L. L.; Tagliazucchi, M., The Phase Behavior of Nanoparticle Superlattices in the Presence of a Solvent. *Acs Nano* **2020,** *14* (5), 5649-5658.
27. Li, Y.; Girard, M.; Shen, M.; Millan, J. A.; Olvera de la Cruz, M., Strong attractions and repulsions mediated by monovalent salts. *Proceedings of the National Academy of Sciences* **2017,** *114* (45), 11838-11843.
28. Kewalramani, S.; Guerrero-García, G. I.; Moreau, L. M.; Zwanikken, J. W.; Mirkin, C. A.; Olvera de la Cruz, M.; Bedzyk, M. J., Electrolyte-Mediated Assembly of Charged Nanoparticles. *ACS Central Science* **2016,** *2* (4), 219-224.
29. Cacace, M. G.; Landau, E. M.; Ramsden, J. J., The Hofmeister series: salt and solvent effects on interfacial phenomena. *Q Rev Biophys* **1997,** *30* (3), 241-277.
30. Jiménez-Ángeles, F.; Odriozola, G.; Lozada-Cassou, M., Electrolyte distribution around two like-charged rods: Their effective attractive interaction and angular dependent charge reversal. *The Journal of Chemical Physics* **2006,** *124* (13), 134902.
31. Qiao, B.; Jiménez-Ángeles, F.; Nguyen, T. D.; Olvera de la Cruz, M., Water follows polar and nonpolar protein surface domains. *Proc Natl Acad Sci U S A* **2019,** *116* (39), 19274-19281.
32. Jiménez-Ángeles, F.; Firoozabadi, A., Hydrophobic Hydration and the Effect of NaCl Salt in the Adsorption of Hydrocarbons and Surfactants on Clathrate Hydrates. *ACS Cent Sci* **2018,** *4* (7), 820-831.
33. Kirkwood, J. G., Statistical Mechanics of Fluid Mixtures. *The Journal of Chemical Physics* **1935,** *3* (5), 300-313.
34. Frenkel, D., *Understanding molecular simulation : from algorithms to applications*. Second edition. San Diego, Calif. ; London : Academic, [2002] ©2002: 2002.
35. Hurst, S. J.; Lytton-Jean, A. K. R.; Mirkin, C. A., Maximizing DNA loading on a range of gold nanoparticle sizes. *Anal Chem* **2006,** *78* (24), 8313-8318.
36. Zhang, L.; Bailey, J. B.; Subramanian, R. H.; Groisman, A.; Tezcan, F. A., Hyperexpandable, self-healing macromolecular crystals with integrated polymer networks. *Nature* **2018,** *557* (7703), 86-91.
37. Brooks, B. R.; Brooks III, C. L.; Mackerell Jr, A. D.; Nilsson, L.; Petrella, R. J.; Roux, B.; Won, Y.; Archontis, G.; Bartels, C.; Boresch, S., CHARMM: the biomolecular simulation program. *Journal of computational chemistry* **2009,** *30* (10), 1545-1614.
38. Lee, J.; Cheng, X.; Swails, J. M.; Yeom, M. S.; Eastman, P. K.; Lemkul, J. A.; Wei, S.; Buckner, J.; Jeong, J. C.; Qi, Y., CHARMM-GUI input generator for NAMD, GROMACS, AMBER, OpenMM, and CHARMM/OpenMM simulations using the CHARMM36 additive force field. *Journal of chemical theory and computation* **2016,** *12* (1), 405-413.
39. Arnott, S.; Smith, P. C.; Chandrasekaran, R., Atomic coordinates and molecular conformations for DNA-DNA, RNA-RNA, and DNA-RNA helices. In *CRC Handbook of biochemistry and molecular biology*, CRC Press: 2019; pp 411-422.
40. Páll, S.; Zhmurov, A.; Bauer, P.; Abraham, M.; Lundborg, M.; Gray, A.; Hess, B.; Lindahl, E., Heterogeneous parallelization and acceleration of molecular dynamics simulations in GROMACS. *The Journal of Chemical Physics* **2020,** *153* (13), 134110.
41. Hess, B.; Kutzner, C.; van der Spoel, D.; Lindahl, E., GROMACS 4: Algorithms for Highly Efficient, Load-Balanced, and Scalable Molecular Simulation. *Journal of Chemical Theory and Computation* **2008,** *4* (3), 435-447.